Supplement of

Investigating fire-induced ozone production from local to global scales

Joseph O. Palmo et al.

Correspondence to: Joseph O. Palmo (jpalmo@mit.edu), Colette L. Heald (colette.heald@env.ethz.ch)

Measurement table

Measurement	Instrument / Method	Campaign(s)	Investigator(s)	Sampling rate	Accuracy	Precision	Reference(s)
O_3, NO, NO_2, NO_y	Chemiluminescence	ARCTAS, WE-CAN	A. Weinheimer	1 Hz	~10%	10 ppt	(Weinheimer et al., 1994)
O_3, NO, NO_2, NO_y	NOAA NOyO3; chemiluminescence	ATom, DC3, FIREX-AQ	T. Ryerson, J. Peischl, I. Bourgeois, C. Thompson, I. Pollack	1 Hz	~10%	~5-10 ppt	(Pollack et al., 2010; Ryerson et al., 2000, 2019)
HNO_3, H_2O_2, HCN	Chemical Ionization Mass Spectrometry (CIMS)	ARCTAS, ATom, DC3, FIREX-AQ	P. Wennberg	10 Hz	±30 %, ±30 %, ±30 %	50 ppt, 50 ppt, 50 ppt	(Crounse et al., 2006; St. Clair et al., 2010)
HCN, HONO	Iodide Ion ToF (Time-of-Flight) CIMS (Chemical Ionization Mass Spectrometer)	WE-CAN	J. Thornton	1 Hz	30%, 30%	112-190ppt, 13.5-23.0ppt	(Lee et al., 2018; Peng et al., 2020)
HONO	Iodide Ion ToF (Time-of-Flight) CIMS (Chemical Ionization Mass Spectrometer)	ATom, FIREX-AQ	P. Veres	1 Hz	±30 %	30 ppt	(Veres et al., 2015)
CO, CH_4	Differential Absorption Carbon monOxide Measurement (DACOM)	DC3, FIREX-AQ, ARCTAS	G. Diskin	5 Hz	±1.5 %	1 ppb	(Diskin et al., 2002; Sachse et al., 1987)
CO, CH_4	Picarro	WE-CAN	T. Campos	5s		15 ppb, 1 ppb	
CO	Picarro Cavity Ringdown	ATom	K. McKain, C. Sweeney	5s		15 ppb, 1 ppb	
CO	Quantum Cascade Laser System (QCLS) Laser	ATom	B. Daube, S. Wofsy, Róisín Commane	1Hz	22 ppb	0.15 ppb	(McManus et al., 2005;

	Absorption Spectrometer						Santoni et al., 2014)
C_2H_6, CH_2O	Laser Absorption Spectroscopy (TDLAS)	DC3, FIREX-AQ, ARCTAS	A. Fried, D. Richter	1 Hz	5%, 6%	18-22 ppt, 28-115 ppt	(Fried et al., 2020; Weibring et al., 2020)
CH_2O	NASA In Situ Airborne Formaldehyde (ISAF)	ATom, DC3, FIREX-AQ	T. Hanisco	1 Hz	10 %	30 ppt	(Cazorla et al., 2015)
Photolysis frequencies	Charge-coupled device actinic flux spectroradiometers (CAFS) and High-performance Instrumented Airborne Platform for Environmental Research (HIAPER) Airborne Radiation Package	ARCTAS, ATom, DC3, FIREX-AQ, WE-CAN	S. Hall, K. Ullman	1 Hz	j_{NO2}: 12%	j_{NO2} 10^{-6} s_{-1}	(Hall et al., 2018;)
Peroxyacetyl nitrate (PAN)	PAN and Trace Hydrohalocarbon ExpeRiment (PANTHER)	ATom	J. Elkins, E. Hintsa	60-120 s	10%	2 ppt ± 10 %	(Wofsy, 2011)
Peroxyacetyl nitrate (PAN)	Chemical Ionization Mass Spectrometer (CIMS)	DC3, FIREX-AQ, ATom, WE-CAN, ARCTAS	G. Huey, F. Flocke	1 Hz			(Zheng et al., 2011)
NMVOCs	Trace Organic Gas Analyzer (TOGA)	ARCTAS, ATom, FIREX, WE-CAN	E. Apel	~35s samples on a 2-minute cycle	~20%	~3%	(Apel et al., 2003)
NMVOCs	Proton-Transfer-Reaction Mass Spectrometer (PTR-ToF-MS)	WE-CAN	L. Hu	0.2-0.5 Hz	Calibrated VOCs: ~10-15%	Mostly at 10s ppt	(Permar et al., 2021)

NMVOCs	Whole Air Sampler (WAS)	ARCTAS, ATom, DC3, FIREX-AQ	D. Blake		~5%	~3%	(Colman et al., 2001; Simpson et al., 2001)
NMVOCs	Whole Air Sampler (WAS)	WE-CAN	J. Collett, A. Sullivan		~5%	~3%	(Colman et al., 2001; Simpson et al., 2001)
NMVOCs	Integrated Whole Air Sampler (iWAS)	FIREX-AQ	J. Gilman	3-10s canister fill rate depending on altitude	6-10%	2-8%	(Lerner et al., 2017)
NMVOCs	High-resolution time-of-flight chemical ionization mass spectrometer utilizing hydronium ions (H3O+ ToF-CIMS)	FIREX-AQ	C. Warneke	1 Hz		20–500 ppt	(Yuan et al., 2016)
NMVOCs	Proton-Transfer-Reaction Mass Spectrometer (PTR-ToF-MS)	FIREX-AQ	A. Wisthaler	1 Hz	10-20%	10-50 ppt	(Müller et al., 2014)
Submicron organic aerosol	HR-ToF-AMS / ToF-AMS	ARCTAS, ATom, DC3, FIREX-AQ	J. L. Jimenez	1 Hz		~2.9 µg sm^{-3}	(Canagaratna et al., 2007; DeCarlo et al., 2006; Guo et al., 2021)
Submicron organic aerosol	HR-ToF-AMS	WE-CAN	D. Farmer	1 Hz		~2.9 µg sm^{-3}	(Garofalo et al., 2019)

Table S1. Measurements used in this study include carbon monoxide (*CO*), nitrogen oxides (*NO$_x$, NO$_y$*), nitric acid (*HNO$_3$*), peroxyacyl nitrates (*PAN*), ozone (*O$_3$*), formaldehyde (*CH$_2$O*), nitrous acid (*HONO*), photolysis rates, organic aerosol concentrations, and a collection of *VOC*s including our fire and anthropogenic *VOC* tracers.

Data cleaning
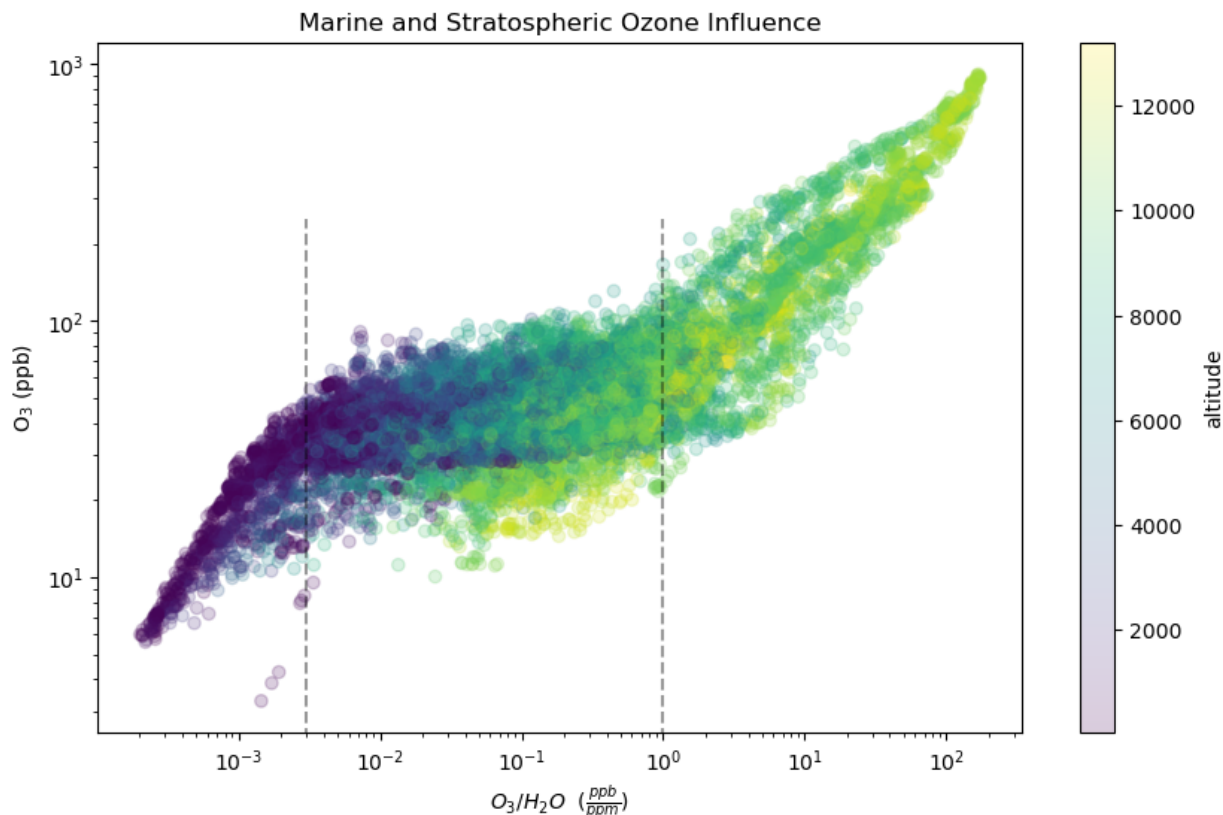
Figure S1. O_3 measurements plotted against the O_3/H_2O ratio in log-log space, colored by altitude, for all five campaigns. The dashed lines represent the stratospheric (O3/H2O = 1 ppb/ppm) and marine (O_3/H_2O = 0.003 ppb/ppm) cutoff values we used, which were defined in (Bourgeois et al., 2021).

Enhancement calculation

The enhancement (Δ) of a given species, X, is defined as follows:

$$\Delta X = [X] - [X]_{background}$$

To obtain enhancements, we first compute background values using the clean subset of points. Because background concentrations vary spatially, our background definition takes under consideration both (1) altitude – by computing background concentrations within 2km altitude bins – and (2) geographic location – by computing background concentrations within different subsets of the clean population:

- Remote – ATom observations

- Arctic – observations that are north of 49° latitude

- Continental – all other observations (continental ARCTAS, DC3, FIREX-AQ, WE-CAN)

The different altitude-dependent backgrounds are shown in Figure S2.
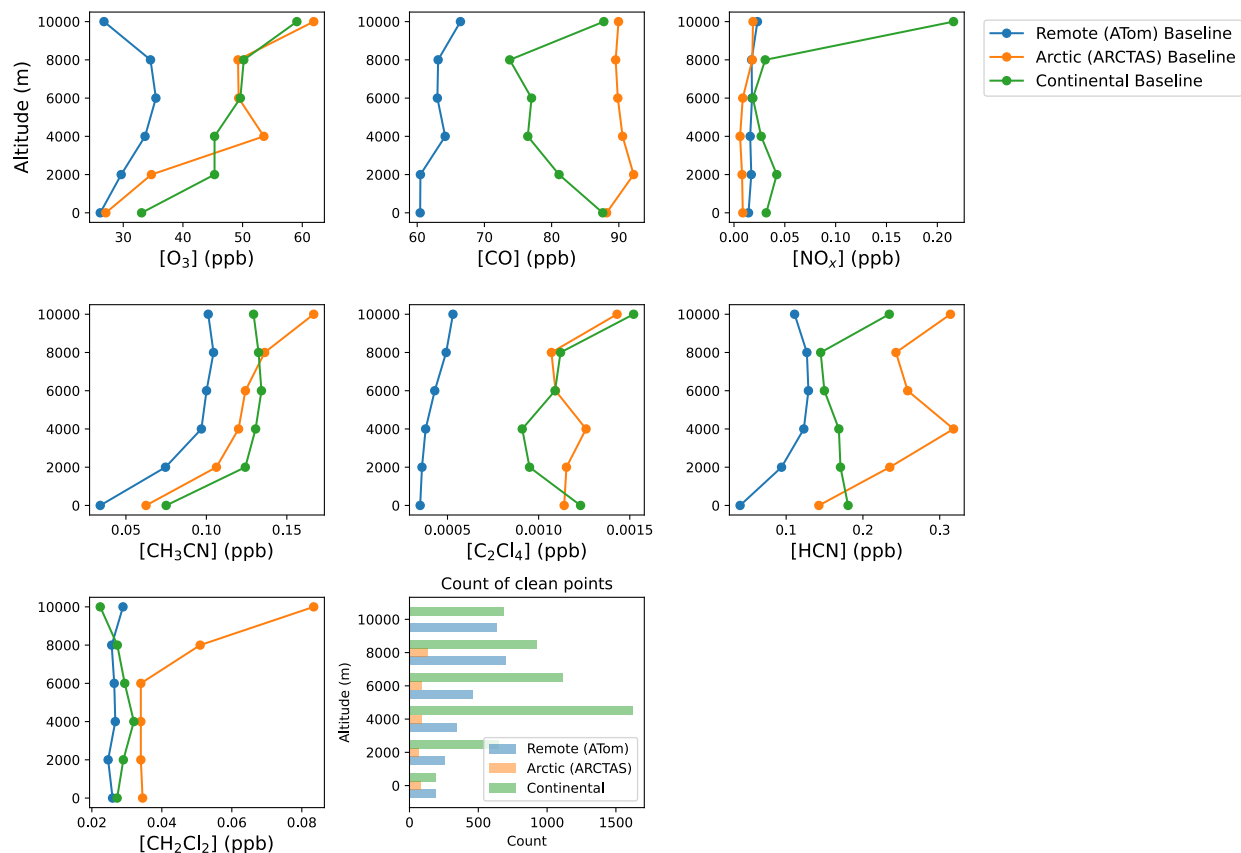
Figure S2. Observed background vertical profiles for clean data points for O3, CO, NOx, CH3CN, C2Cl4, HCN, and CH2Cl2. The bottom panel shows the vertical distribution of points within each subset of the clean population.

Model background concentrations were computed in the same way as the observations, except we filtered clean points based on the observationally defined chemical regimes. Model clean points ([CO]$_{model}$ < [CO]$_{model, 40th \, percentile}$) were only included in the background calculation if they were also defined as clean in the observations ([CO]$_{obs}$ < [CO]$_{obs, 40th \, percentile}$).
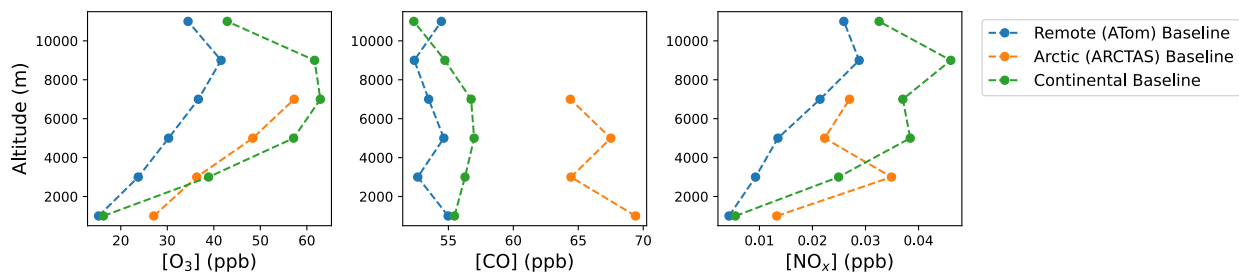
Figure S3. Modeled background vertical profile for clean data points sampled from GEOS-Chem, for O3, CO, and NOx.

Regime definition
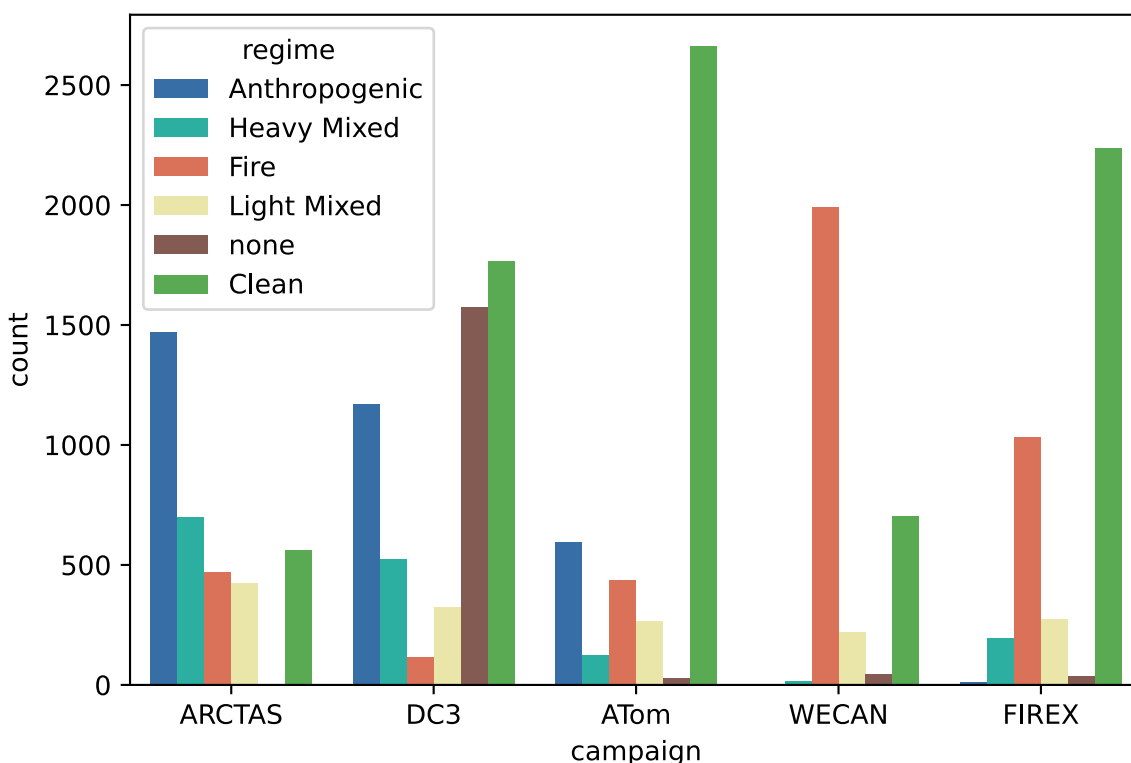
Figure S4. Breakdown of defined regimes across different campaigns. The 'none' regime represents data points where no valid tracer measurement exists for quantifying fire (CH3CN, HCN) or anthropogenic (C2Cl4, CH2Cl2) influence.

Photochemical aging

The photochemical age of fire-influenced observations was computed with Equation (1):

$$\Delta t = \frac{1}{[OH] * (k_X - k_Y)} * \left[\ln\left(\frac{X}{Y}\right) \Big|_{t=0} - \ln\left(\frac{X}{Y}\right) \right] \tag{1}$$
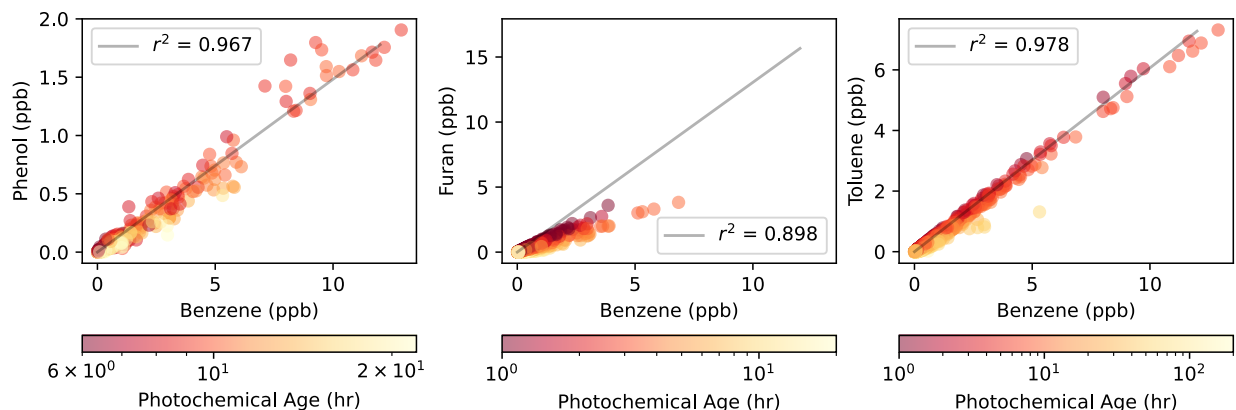
Figure S5. Scatterplots with reduced major axis regression best fit lines and correlation coefficients for each photochemical age ratio we used. The x-axis corresponds to benzene for each plot, which is the denominator (Y) VOC in Equation (1), while the y-axis corresponds to the more reactive numerator (X) VOC.
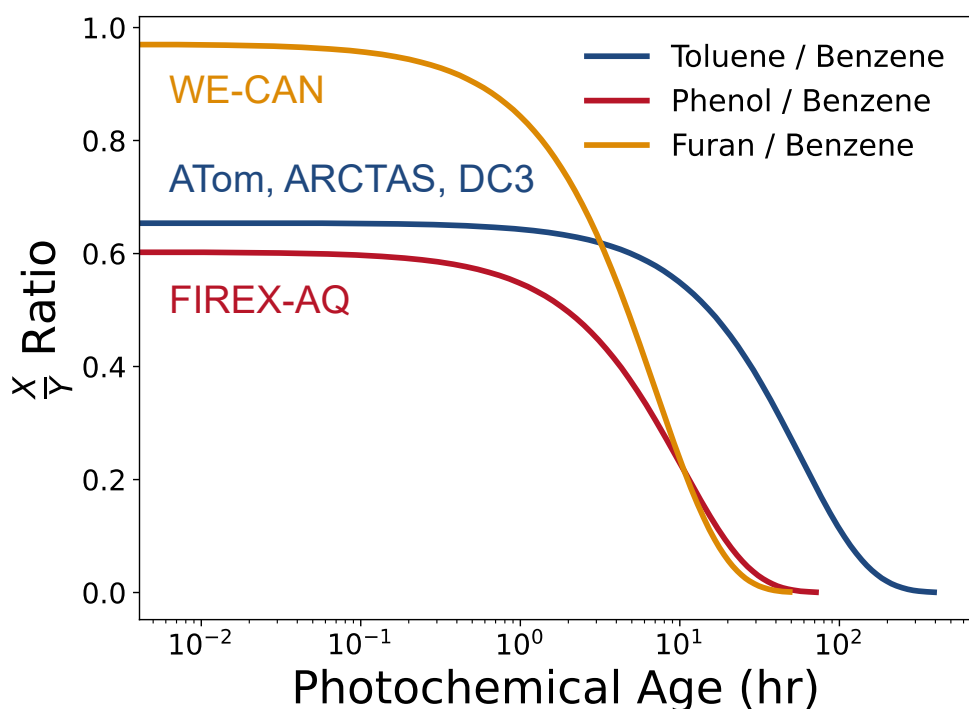
Figure S6. The ratio between X and Y VOCs in Equation (1) plotted against the corresponding photochemical age, computed assuming an average OH concentration of $10^6 \frac{molec}{cm^2}$.. The three different ratios we used in this work are represented with different color lines, with the campaign(s) each ratio was employed for listed alongside each line. The slope of the curves reflects the sensitivity each ratio has to different smoke ages – phenol and furan are shorter-lived, therefore more sensitive to near-field aging, whereas toluene is longer-lived and more sensitive to far-field aging.

Observed ozone formation regime transition
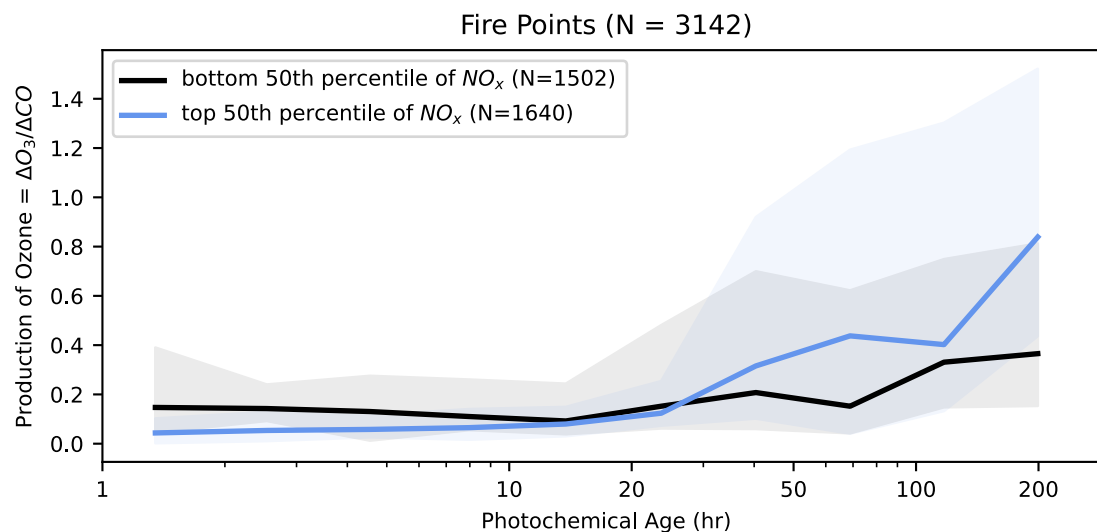
Figure S7. Observed ozone production (ΔO3/ΔCO) plotted across 11 evenly log-spaced bins of photochemical age for all fire-influenced observations, split at the 50th percentile of NOx. The blue trace represents the median of the top 50th percentile points within each bin, while the shaded area extends from the 16th to the 84th percentile (corresponding to one standard deviation, but in outlier resistant percentile space) within each bin. The black trace represents the same, but for points below the 50th percentile of NOx.
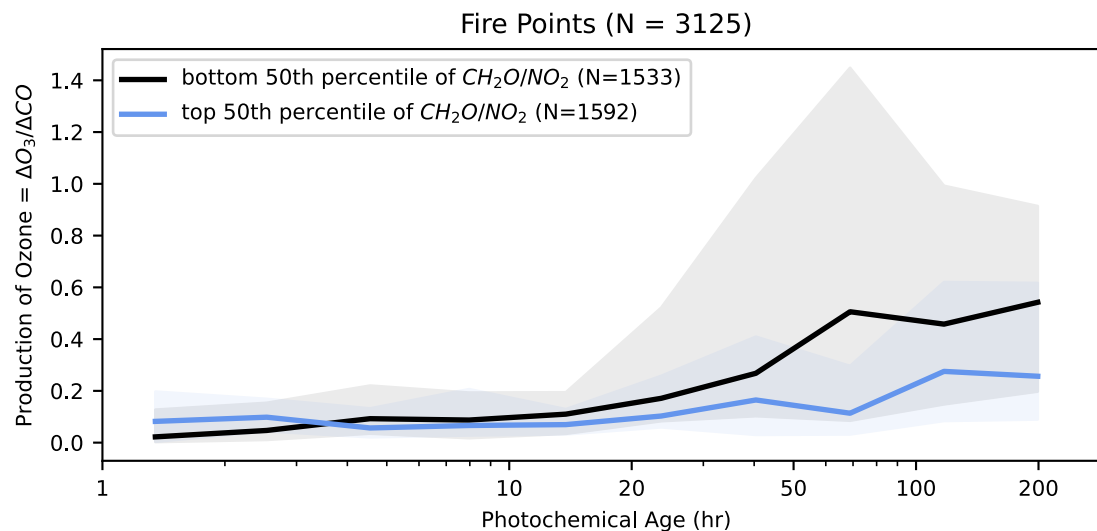
Figure S8. Observed ozone Production (ΔO3/ΔCO) plotted across 11 evenly log-spaced bins of photochemical age for all fire-influenced observations, split at the 50th percentile of CH2O/NO2. The blue trace represents the median of the top 50th percentile points within each bin, while the shaded area extends from the 16th to the 84th percentile (corresponding to one standard deviation, but in outlier resistant percentile space) within each bin. The black trace represents the same, but for points below the 50th percentile of CH2O/NO2.

Box model description

Aerosol treatment

To simulate modulating photolysis rates within smoke, we scale observed jNO2 values against the default, clear sky jNO2 value calculated with the MCM photolysis parameterization. We note that brown carbon aerosols within the smoke increases absorption with decreasing ultraviolet wavelengths (Laskin et al., 2015), a spectral region where photolysis frequencies are strongly spectrally dependent. Thus, scaling other photolysis frequencies to jNO2 induces some biases. From this scaling we receive a distribution of ratios that we assume describes the potential relative light intensity, *I*, observed within a plume at a single moment. To test the sensitivity of the chemical system to this light intensity, for each Monte Carlo run we randomly draw a value from the *I* distribution and scale all our photolysis rates by that ratio (if it is greater than 1, we assume it is 1). For the "time-of-emission" population, we use the near-field distribution of light intensities. To estimate the range of smoke aerosol surface area observed, we derive *SA* from organic aerosol mass concentration measurements, assuming a constant specific surface area of 4 $m^2 \, g^{-1}$ following (Lindsay et al., 2022).

The heterogeneous uptake of HO2 onto aerosol is represented in the box model in the same fashion as GEOS-Chem – using a reaction probability parameterization (Jacob 2000). In the case of smoke aerosol, gas uptake tends to be limited by the free molecular collision rate (Sutugxn et al., n.d.), rather than diffusion, meaning the uptake rate is given to a good approximation by:

$$k = \frac{1}{4} * \gamma * \bar{c}_{HO_2} * SA$$

In the above equation $\bar{c}_{HO_2}$ represents the mean molecular speed of HO_2, γ corresponds to the heterogeneous uptake coefficient for HO_2. The rate of heterogeneous uptake, k, is proportional to the surface area of biomass burning aerosol, *SA*.

VOCR calculation

VOC reactivity (VOCR) is a metric that describes the population of organic gases in terms of ambient OH loss. It is typically used as a proxy for total peroxy radical formation and ozone formation regime. VOCR is formulated as:

$$VOCR = \sum_i k_{OH+X_i}[X_i]$$

where X represents a VOC. Because of unmeasured VOCs, the total VOCR is higher than that calculated with measurements (VOCR$_m$). Across our suite of campaigns, the number of measured VOCs varies, meaning the calculated VOCR$_m$ for each campaign cannot be robustly compared against another. To combat this limitation, we choose a subset of VOCs that is reliably measured in every campaign and compute a reduced form reactivity metric based on those VOCs, called VOCR$_t$. The subset of VOCs was chosen based on availability, importance in smoke, and their assumed contribution to total OHR: [CO, CH4, Ethene, CH2O, Propane, Isoprene, Furan, Benzene, Toluene]. Seemingly regardless the level of specificity / number of VOCs included in VOCR$_t$, the relative magnitudes of VOCR$_t$ across regimes were consistent. So, though it is qualitatively chosen, our VOCR$_t$ is meant to reflect the cross-regime differences, and we conclude that it does.

Fire-anthropogenic mixing
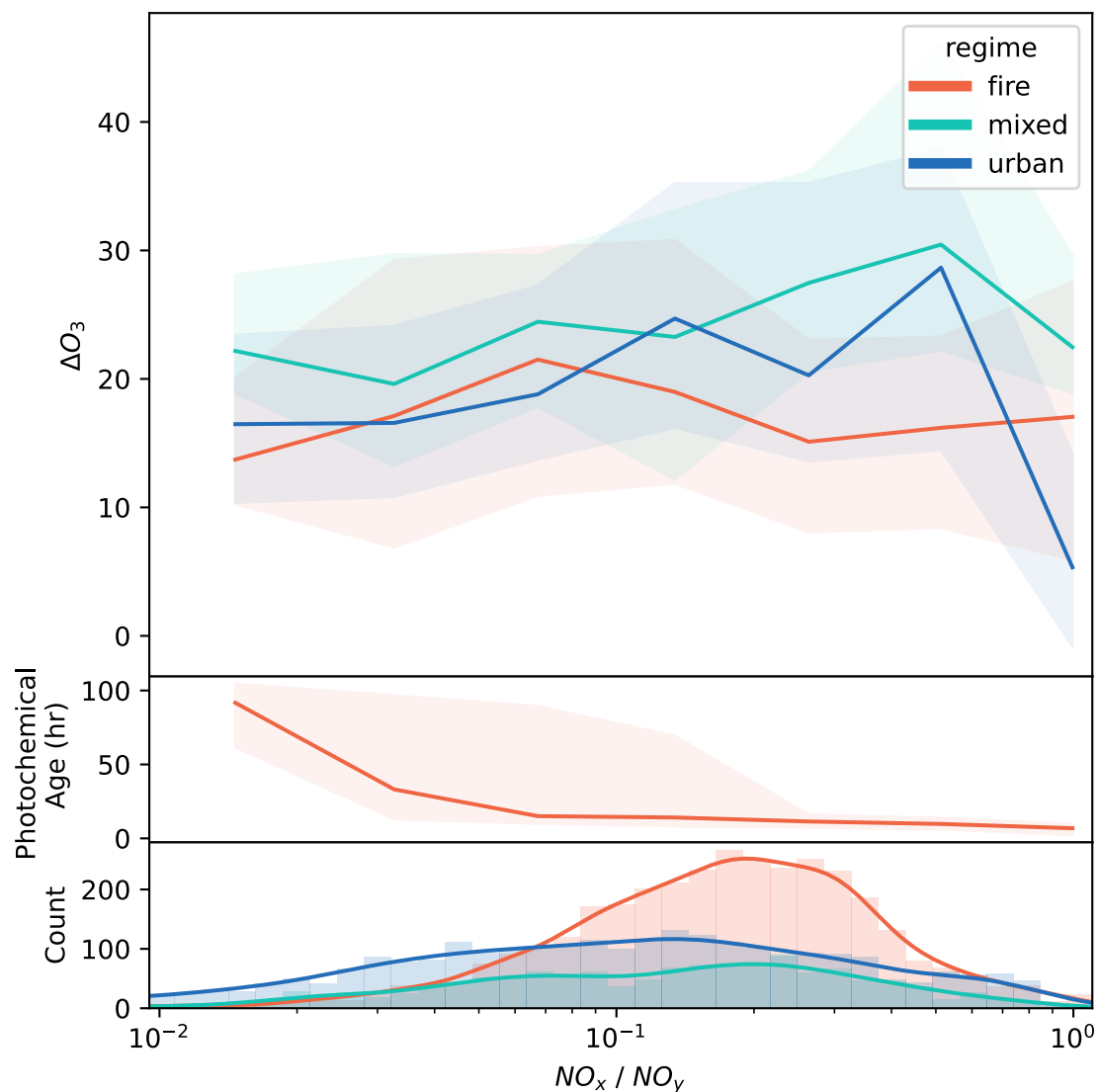
Figure S9. (top) Ozone enhancements (ΔO3) vs. NOx/NOy across fire, urban, and mixed regimes. (middle) Photochemical age vs. NOx/NOy for fire-influenced points. (bottom) Histogram of NOx/NOy across fire, urban, and mixed regimes.

Based on Figure 6, we define the subset of our mixed population that has both ΔNOx / ΔCH3CN > 3 and ΔC2Cl4 concentrations above the mixed median as mixed$_{anthro}$, and the rest of the mixed observations as mixed$_{fire}$. We find that on average, within mixed$_{anthro}$ ΔNOx is over a factor of 4 higher than it is within mixed$_{fire}$, amounting to an enhancement of just over 2 ppb. This additional anthropogenic NOx leads to a mean mixed$_{anthro}$ ΔO3 of ~42 ppb, nearly double that of mixed$_{fire}$ (~24 ppb). Also notable is that within this mixed$_{anthro}$ population, PAN is enhanced by

0.8 ppb compared to the mixed$_{fire}$ mean of 0.6 ppb, meaning the injection of anthropogenic NOx contributes to additional secondary PAN formation that could result in further ozone enhancements downwind.
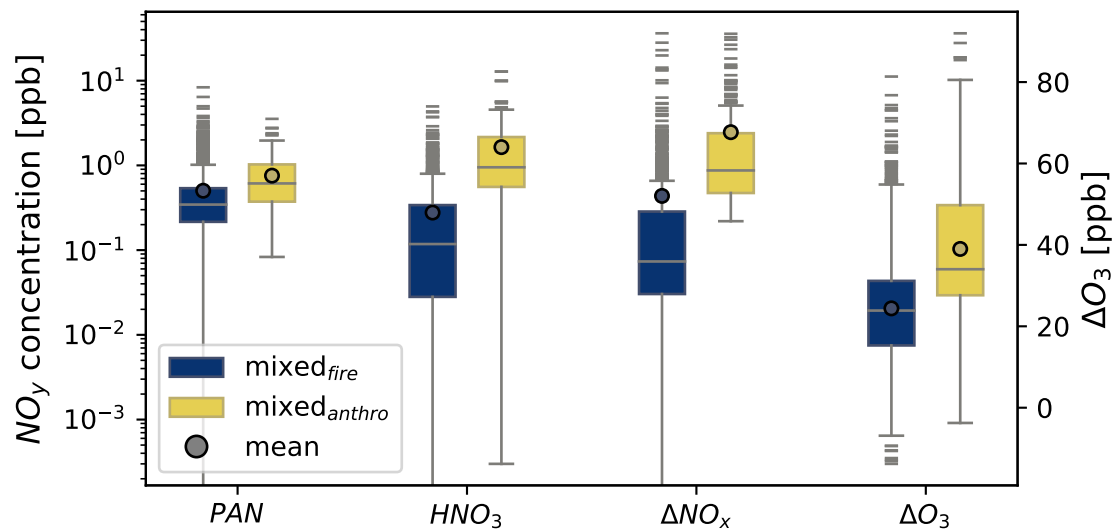
Figure S10. Comparison of various quantities between mixed$_{fire}$ and mixed$_{anthro}$ population. Left y-axis corresponds to NOy species PAN, HNO3, and ΔNOx, while the right y-axis corresponds to ΔO3.

Model Evaluation

Nested vs. coarse
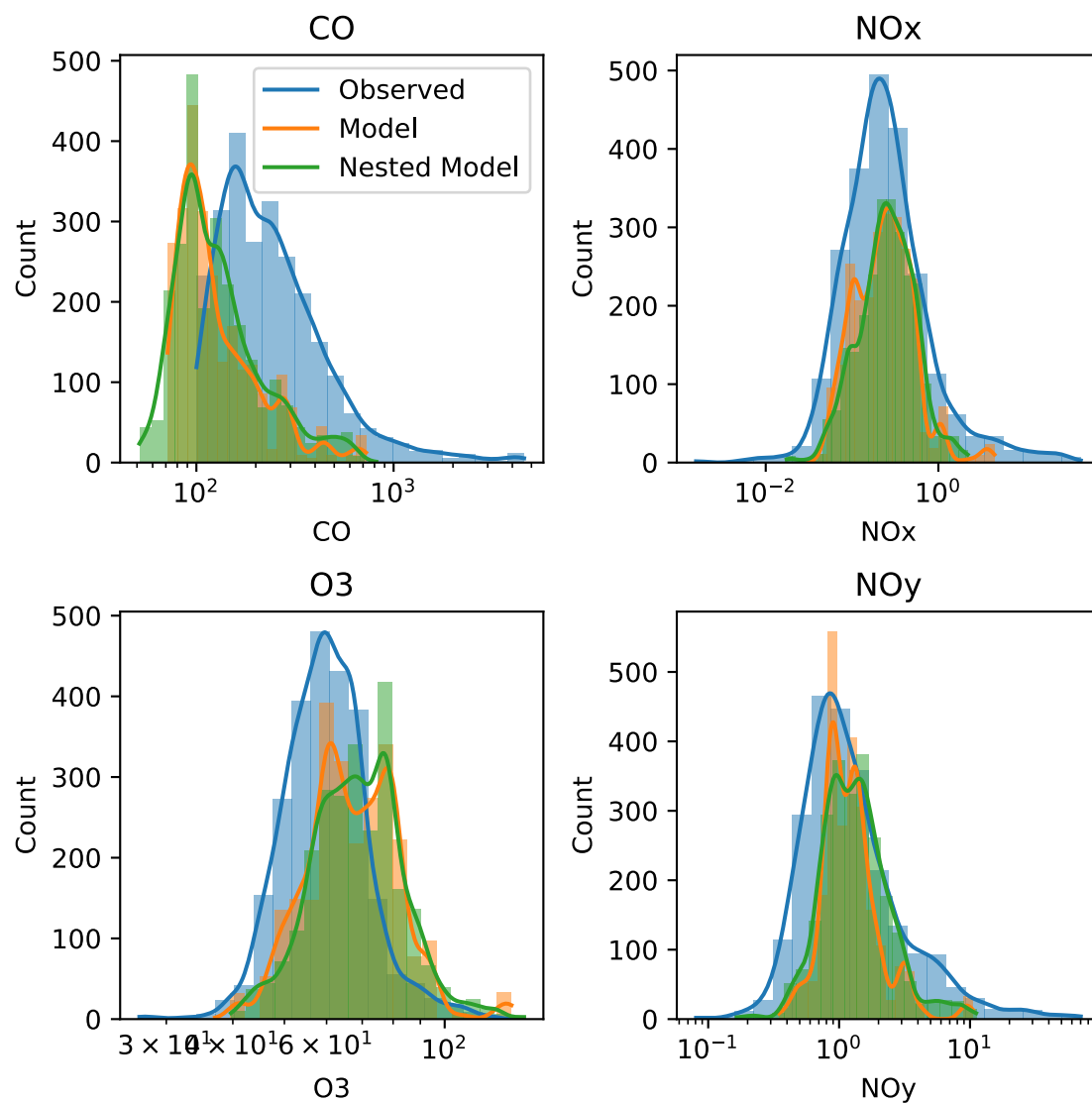
Figure S11. Distribution of concentrations for different species observed (blue), and modeled at coarse resolution (2°x2.5°; orange) and nested resolution (0.5°x0.625°; green).

NOx sensitivity
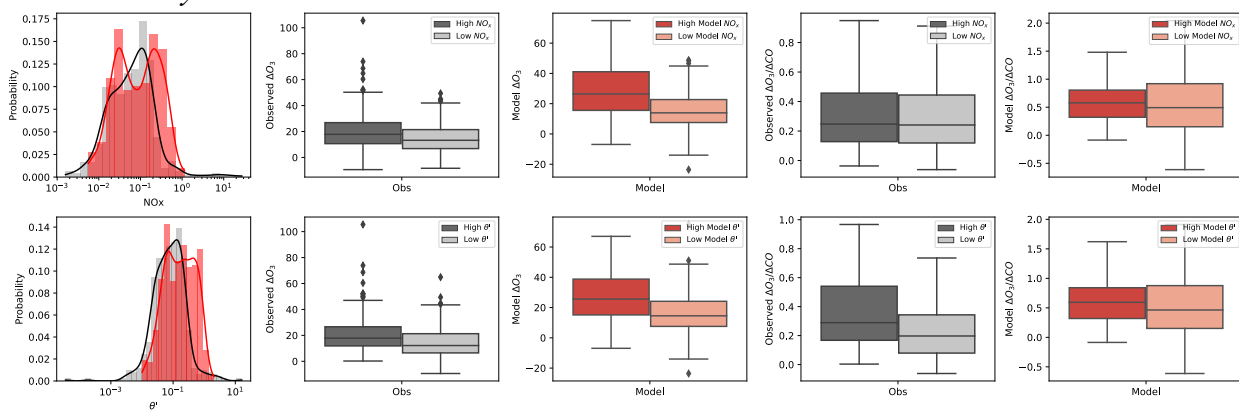
Figure S12. The differences in ozone sensitivity to NOx in the model versus the observations, in terms of two different metrics: ΔNOx (top row) and θ' (bottom row). The left column shows the observed (black) and modeled (red) distribution of each respective metric. The second column shows the observed distribution of ΔO3 for both the observed bottom ("low") and top ("high") 50th percentile of each metric. The third column shows the modeled distribution of ΔO3 for both the modeled bottom ("low") and top ("high") 50th percentile of each metric. This pattern is repeated in the last two columns for the distribution of ΔO3/ΔCO.
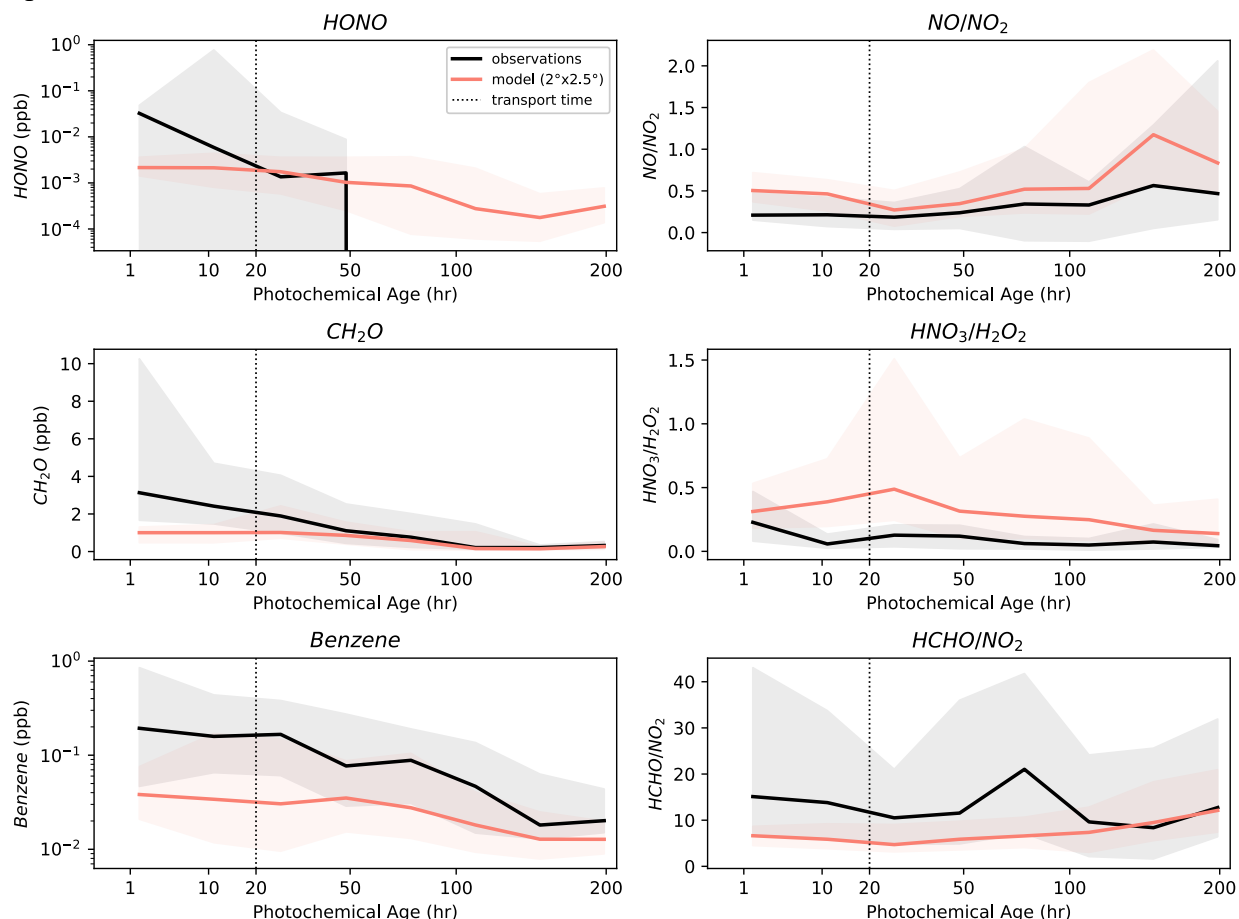
Figure S13. Comparison between GEOS-Chem simulated (red) and our fire-influenced observations (black), plotted over observationally-derived photochemical ages, binned in log-space. The lines represent the median, and the shaded area extends from the 16th to the 84th percentile (corresponding to one standard deviation, in outlier resistant percentile space) within each bin. The dashed line represents the approximate transport time for a 2°x2.5° grid box at mid-latitudes.

Reactive Nitrogen Partitioning
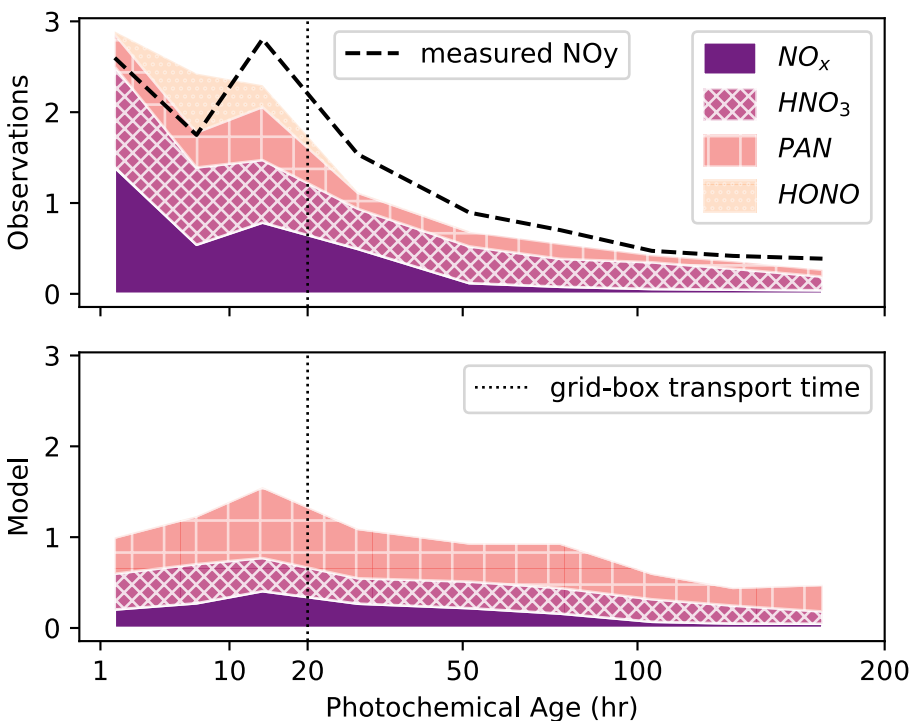
Figure S14. Mean NO_y speciation of fire-influenced points plotted over smoke age for both observations (top) and GEOS-Chem (bottom). The measured total NOy (from chemiluminescence) value is overplotted with the dashed black line.

Global fire-ozone impact

Using the year 2020 as a case study, we quantify the overall impact that fires have in governing the tropospheric ozone burden in the GEOS-Chem model. In Figure 9a, we compute the percentage of the tropospheric ozone burden that can be attributed to fire in the model. To make this calculation, we define the tropopause as the 35th hybrid sigma-pressure level in GEOS-Chem, corresponding to about 100 hPa. In Figure 9c, we compute the population-weighted surface ozone exposure percentage that can be attributed to fire in the model. This requires gridded population data, which we obtained from the Columbia Center for Integrated Earth System Information (CIESIN) produced product that was hosted by the NASA Socioeconomic Data and Applications Center (SEDAC) until March 2025. The product was offered in 1°x1° resolution, which we regridded to match the GEOS-Chem grid (2°x2.5°).

References:

Apel, E. C., Hills, A. J., Lueb, R., Zindel, S., Eisele, S., and Riemer, D. D.: A fast-GC/MS system to measure C2 to C4 carbonyls and methanol aboard aircraft, Journal of Geophysical Research: Atmospheres, 108, https://doi.org/10.1029/2002JD003199, 2003.

Bourgeois, I., Peischl, J., Neuman, J. A., Brown, S. S., Thompson, C. R., Aikin, K. C., Allen, H. M., Angot, H., Apel, E. C., Baublitz, C. B., Brewer, J. F., Campuzano-Jost, P., Commane, R., Crounse, J. D., Daube, B. C., DiGangi, J. P., Diskin, G. S., Emmons, L. K., Fiore, A. M., Gkatzelis, G. I., Hills, A., Hornbrook, R. S., Huey, L. G., Jimenez, J. L., Kim, M., Lacey, F., McKain, K., Murray, L. T., Nault, B. A., Parrish, D. D., Ray, E., Sweeney, C., Tanner, D., Wofsy, S. C., and Ryerson, T. B.: Large contribution of biomass burning emissions to ozone throughout the global remote troposphere, Proc. Natl. Acad. Sci. U.S.A., 118, e2109628118, https://doi.org/10.1073/pnas.2109628118, 2021.

Canagaratna, M. R., Jayne, J. T., Jimenez, J. L., Allan, J. D., Alfarra, M. R., Zhang, Q., Onasch, T. B., Drewnick, F., Coe, H., Middlebrook, A., Delia, A., Williams, L. R., Trimborn, A. M., Northway, M. J., DeCarlo, P. F., Kolb, C. E., Davidovits, P., and Worsnop, D. R.: Chemical and microphysical characterization of ambient aerosols with the aerodyne aerosol mass spectrometer, Mass Spectrom Rev, 26, 185–222, https://doi.org/10.1002/mas.20115, 2007.

Cazorla, M., Wolfe, G. M., Bailey, S. A., Swanson, A. K., Arkinson, H. L., and Hanisco, T. F.: A new airborne laser-induced fluorescence instrument for in situ detection of formaldehyde throughout the troposphere and lower stratosphere, Atmospheric Measurement Techniques, 8, 541–552, https://doi.org/10.5194/amt-8-541-2015, 2015.

Colman, J. J., Swanson, A. L., Meinardi, S., Sive, B. C., Blake, D. R., and Rowland, F. S.: Description of the Analysis of a Wide Range of Volatile Organic Compounds in Whole Air Samples Collected during PEM-Tropics A and B, Anal. Chem., 73, 3723–3731, https://doi.org/10.1021/ac010027g, 2001.

Crounse, J. D., McKinney, K. A., Kwan, A. J., and Wennberg, P. O.: Measurement of Gas-Phase Hydroperoxides by Chemical Ionization Mass Spectrometry, Anal. Chem., 78, 6726–6732, https://doi.org/10.1021/ac0604235, 2006.

DeCarlo, P. F., Kimmel, J. R., Trimborn, A., Northway, M. J., Jayne, J. T., Aiken, A. C., Gonin, M., Fuhrer, K., Horvath, T., Docherty, K. S., Worsnop, D. R., and Jimenez, J. L.: Field-Deployable, High-Resolution, Time-of-Flight Aerosol Mass Spectrometer, Anal. Chem., 78, 8281–8289, https://doi.org/10.1021/ac061249n, 2006.

Diskin, G. S., Podolske, J. R., Sachse, G. W., and Slate, T. A.: Open-path airborne tunable diode laser hygrometer, in: Diode Lasers and Applications in Atmospheric Sensing, Diode Lasers and Applications in Atmospheric Sensing, 196–204, https://doi.org/10.1117/12.453736, 2002.

Fried, A., Walega, J., Weibring, P., Richter, D., Simpson, I. J., Blake, D. R., Blake, N. J., Meinardi, S., Barletta, B., Hughes, S. C., Crawford, J. H., Diskin, G., Barrick, J., Hair, J., Fenn, M., Wisthaler, A., Mikoviny, T., Woo, J.-H., Park, M., Kim, J., Min, K.-E., Jeong, S., Wennberg,

P. O., Kim, M. J., Crounse, J. D., Teng, A. P., Bennett, R., Yang-Martin, M., Shook, M. A., Huey, G., Tanner, D., Knote, C., Kim, J., Park, R., and Brune, W.: Airborne formaldehyde and volatile organic compound measurements over the Daesan petrochemical complex on Korea's northwest coast during the Korea-United States Air Quality study: Estimation of emission fluxes and effects on air quality, Elementa: Science of the Anthropocene, 8, 121, https://doi.org/10.1525/elementa.2020.121, 2020.

Garofalo, L. A., Pothier, M. A., Levin, E. J. T., Campos, T., Kreidenweis, S. M., and Farmer, D. K.: Emission and Evolution of Submicron Organic Aerosol in Smoke from Wildfires in the Western United States, ACS Earth Space Chem., 3, 1237–1247, https://doi.org/10.1021/acsearthspacechem.9b00125, 2019.

Guo, H., Campuzano-Jost, P., Nault, B. A., Day, D. A., Schroder, J. C., Kim, D., Dibb, J. E., Dollner, M., Weinzierl, B., and Jimenez, J. L.: The importance of size ranges in aerosol instrument intercomparisons: a case study for the Atmospheric Tomography Mission, Atmospheric Measurement Techniques, 14, 3631–3655, https://doi.org/10.5194/amt-14-3631-2021, 2021.

Hall, S. R., Ullmann, K., Prather, M. J., Flynn, C. M., Murray, L. T., Fiore, A. M., Correa, G., Strode, S. A., Steenrod, S. D., Lamarque, J.-F., Guth, J., Josse, B., Flemming, J., Huijnen, V., Abraham, N. L., and Archibald, A. T.: Cloud impacts on photochemistry: building a climatology of photolysis rates from the Atmospheric Tomography mission, Atmospheric Chemistry and Physics, 18, 16809–16828, https://doi.org/10.5194/acp-18-16809-2018, 2018.

Jacob, D. J.: Heterogeneous chemistry and tropospheric ozone, Atmospheric Environment, 34, 2131–2159, https://doi.org/10.1016/S1352-2310(99)00462-8, 2000.

Laskin, A., Laskin, J., and Nizkorodov, S. A.: Chemistry of Atmospheric Brown Carbon, Chem. Rev., 115, 4335–4382, https://doi.org/10.1021/cr5006167, 2015.

Lee, B. H., Lopez-Hilfiker, F. D., Veres, P. R., McDuffie, E. E., Fibiger, D. L., Sparks, T. L., Ebben, C. J., Green, J. R., Schroder, J. C., Campuzano-Jost, P., Iyer, S., D'Ambro, E. L., Schobesberger, S., Brown, S. S., Wooldridge, P. J., Cohen, R. C., Fiddler, M. N., Bililign, S., Jimenez, J. L., Kurtén, T., Weinheimer, A. J., Jaegle, L., and Thornton, J. A.: Flight Deployment of a High-Resolution Time-of-Flight Chemical Ionization Mass Spectrometer: Observations of Reactive Halogen and Nitrogen Oxide Species, Journal of Geophysical Research: Atmospheres, 123, 7670–7686, https://doi.org/10.1029/2017JD028082, 2018.

Lerner, B. M., Gilman, J. B., Aikin, K. C., Atlas, E. L., Goldan, P. D., Graus, M., Hendershot, R., Isaacman-VanWertz, G. A., Koss, A., Kuster, W. C., Lueb, R. A., McLaughlin, R. J., Peischl, J., Sueper, D., Ryerson, T. B., Tokarek, T. W., Warneke, C., Yuan, B., and de Gouw, J. A.: An improved, automated whole air sampler and gas chromatography mass spectrometry analysis system for volatile organic compounds in the atmosphere, Atmospheric Measurement Techniques, 10, 291–313, https://doi.org/10.5194/amt-10-291-2017, 2017.

Lindsay, A. J., Anderson, D. C., Wernis, R. A., Liang, Y., Goldstein, A. H., Herndon, S. C., Roscioli, J. R., Dyroff, C., Fortner, E. C., Croteau, P. L., Majluf, F., Krechmer, J. E., Yacovitch, T. I., Knighton, W. B., and Wood, E. C.: Ground-based investigation of HO_x and ozone chemistry

in biomass burning plumes in rural Idaho, Atmospheric Chemistry and Physics, 22, 4909–4928, https://doi.org/10.5194/acp-22-4909-2022, 2022.

McManus, J. B., Nelson, D. D., Shorter, J. H., Jimenez, R., Herndon, S., Saleska, S., and Zahniser, M.: A high precision pulsed quantum cascade laser spectrometer for measurements of stable isotopes of carbon dioxide, Journal of Modern Optics, 52, 2309–2321, https://doi.org/10.1080/09500340500303710, 2005.

Müller, M., Mikoviny, T., Feil, S., Haidacher, S., Hanel, G., Hartungen, E., Jordan, A., Märk, L., Mutschlechner, P., Schottkowsky, R., Sulzer, P., Crawford, J. H., and Wisthaler, A.: A compact PTR-ToF-MS instrument for airborne measurements of volatile organic compounds at high spatiotemporal resolution, Atmospheric Measurement Techniques, 7, 3763–3772, https://doi.org/10.5194/amt-7-3763-2014, 2014.

Peng, Q., Palm, B. B., Melander, K. E., Lee, B. H., Hall, S. R., Ullmann, K., Campos, T., Weinheimer, A. J., Apel, E. C., Hornbrook, R. S., Hills, A. J., Montzka, D. D., Flocke, F., Hu, L., Permar, W., Wielgasz, C., Lindaas, J., Pollack, I. B., Fischer, E. V., Bertram, T. H., and Thornton, J. A.: HONO Emissions from Western U.S. Wildfires Provide Dominant Radical Source in Fresh Wildfire Smoke, Environ. Sci. Technol., 54, 5954–5963, https://doi.org/10.1021/acs.est.0c00126, 2020.

Petropavlovskikh, I., Froidevaux, L., Shetter, R., Hall, S., Ullmann, K., Bhartia, P. K., Kroon, M., and Levelt, P.: In-flight validation of Aura MLS ozone with CAFS partial ozone columns, Journal of Geophysical Research: Atmospheres, 113, https://doi.org/10.1029/2007JD008690, 2008.

Pollack, I. B., Lerner, B. M., and Ryerson, T. B.: Evaluation of ultraviolet light-emitting diodes for detection of atmospheric NO2 by photolysis - chemiluminescence, J Atmos Chem, 65, 111–125, https://doi.org/10.1007/s10874-011-9184-3, 2010.

Ryerson, T. B., Williams, E. J., and Fehsenfeld, F. C.: An efficient photolysis system for fast-response NO2 measurements, Journal of Geophysical Research: Atmospheres, 105, 26447–26461, https://doi.org/10.1029/2000JD900389, 2000.

Ryerson, T. B., Thompson, C. R., Peischl, J., and Bourgeois, I.: ATom: L2 In Situ Measurements from NOAA Nitrogen Oxides and Ozone (NOyO3) Instrument, ORNL DAAC, https://doi.org/10.3334/ORNLDAAC/1734, 2019.

Sachse, G. W., Hill, G. F., Wade, L. O., and Perry, M. G.: Fast-response, high-precision carbon monoxide sensor using a tunable diode laser absorption technique, Journal of Geophysical Research: Atmospheres, 92, 2071–2081, https://doi.org/10.1029/JD092iD02p02071, 1987.

Santoni, G. W., Daube, B. C., Kort, E. A., Jiménez, R., Park, S., Pittman, J. V., Gottlieb, E., Xiang, B., Zahniser, M. S., Nelson, D. D., McManus, J. B., Peischl, J., Ryerson, T. B., Holloway, J. S., Andrews, A. E., Sweeney, C., Hall, B., Hintsa, E. J., Moore, F. L., Elkins, J. W., Hurst, D. F., Stephens, B. B., Bent, J., and Wofsy, S. C.: Evaluation of the airborne quantum cascade laser spectrometer (QCLS) measurements of the carbon and greenhouse gas suite – CO_2 , CH_4 , $N_2 O$,

and CO – during the CalNex and HIPPO campaigns, Atmos. Meas. Tech., 7, 1509–1526, https://doi.org/10.5194/amt-7-1509-2014, 2014.

Shetter, R. E. and Müller, M.: Photolysis frequency measurements using actinic flux spectroradiometry during the PEM-Tropics mission: Instrumentation description and some results, Journal of Geophysical Research: Atmospheres, 104, 5647–5661, https://doi.org/10.1029/98JD01381, 1999.

Simpson, I. J., Colman, J. J., Swanson, A. L., Bandy, A. R., Thornton, D. C., Blake, D. R., and Rowland, F. S.: Aircraft Measurements of Dimethyl Sulfide (DMS) Using a Whole Air Sampling Technique, Journal of Atmospheric Chemistry, 39, 191–213, https://doi.org/10.1023/A:1010608529779, 2001.

St. Clair, J. M., McCabe, D. C., Crounse, J. D., Steiner, U., and Wennberg, P. O.: Chemical ionization tandem mass spectrometer for the in situ measurement of methyl hydrogen peroxide, Review of Scientific Instruments, 81, 094102, https://doi.org/10.1063/1.3480552, 2010.

Sutugxn, A. G., Fucns, N. A., and Kotsev, E. I.: FORMATION OF CONDENSATION AEROSOLS UNDER RAPIDLY CHANGING ENVIRONMENTAL CONDITIONS, n.d.

Veres, P. R., Roberts, J. M., Wild, R. J., Edwards, P. M., Brown, S. S., Bates, T. S., Quinn, P. K., Johnson, J. E., Zamora, R. J., and de Gouw, J.: Peroxynitric acid (HO_2NO_2) measurements during the UBWOS 2013 and 2014 studies using iodide ion chemical ionization mass spectrometry, Atmospheric Chemistry and Physics, 15, 8101–8114, https://doi.org/10.5194/acp-15-8101-2015, 2015.

Weibring, P., Richter, D., Walega, J. G., Fried, A., DiGangi, J., Halliday, H., Choi, Y., Baier, B., Sweeney, C., Miller, B., Davis, K. J., Barkley, Z., and Obland, M. D.: Autonomous airborne mid-infrared spectrometer for high-precision measurements of ethane during the NASA ACT-America studies, Atmospheric Measurement Techniques, 13, 6095–6112, https://doi.org/10.5194/amt-13-6095-2020, 2020.

Weinheimer, A. J., Walega, J. G., Ridley, B. A., Gary, B. L., Blake, D. R., Blake, N. J., Rowland, F. S., Sachse, G. W., Anderson, B. E., and Collins, J. E.: Meridional distributions of NOx, NOy, and other species in the lower stratosphere and upper troposphere during AASE II, Geophysical Research Letters, 21, 2583–2586, https://doi.org/10.1029/94GL01897, 1994.

Wofsy, S. C.: HIAPER Pole-to-Pole Observations (HIPPO): fine-grained, global-scale measurements of climatically important atmospheric gases and aerosols, Philosophical Transactions of the Royal Society A: Mathematical, Physical and Engineering Sciences, 369, 2073–2086, https://doi.org/10.1098/rsta.2010.0313, 2011.

Yuan, B., Koss, A., Warneke, C., Gilman, J. B., Lerner, B. M., Stark, H., and de Gouw, J. A.: A high-resolution time-of-flight chemical ionization mass spectrometer utilizing hydronium ions (H_3O^+ ToF-CIMS) for measurements of volatile organic compounds in the atmosphere, Atmospheric Measurement Techniques, 9, 2735–2752, https://doi.org/10.5194/amt-9-2735-2016, 2016.

Zheng, W., Flocke, F. M., Tyndall, G. S., Swanson, A., Orlando, J. J., Roberts, J. M., Huey, L. G., and Tanner, D. J.: Characterization of a thermal decomposition chemical ionization mass spectrometer for the measurement of peroxy acyl nitrates (PANs) in the atmosphere, Atmospheric Chemistry and Physics, 11, 6529–6547, https://doi.org/10.5194/acp-11-6529-2011, 2011.